IEEE Robotics and Automation Letters (RA-L) paper, presented at ICRA 2026, Vienna, Austria. Cite as RA-L paper.

ATOM: A Tendon-Driven Aerial Manipulator Achieving High Stiffness, High Torque, and Low Coupling Disturbance

Quman Xu, *Student Member, IEEE*, Zhan Li, *Member, IEEE*, Hai Li, *Member, IEEE*, Yipeng Yang, *Member, IEEE*, Xinghu Yu, *Member, IEEE*, and Zhang Chen,*Member, IEEE*

***Abstract*—Aerial manipulator systems (AMSs) have significantly progressed in air-ground collaborative tasks. Deploying high-stiffness and high-torque manipulators in AMSs can enhance operational robustness, enabling the execution of more demanding tasks such as high-altitude platforms operation, post-disaster rapid response and assisted rescue. However, this is challenging due to the significant coupling disturbance (CPD) induced by the substantial mass and inertia of high-torque joint actuators. To address this issue, we introduce the aerial tendon-driven manipulator (ATOM), which integrates a multirotor with a 4-DOF anthropomorphic tendon-driven serial manipulator. This design minimizes CPD while preserving high-stiffness and high-torque. Our approach begins with an analysis of the CPD model inherent in AMSs, guiding the development of our design concept. In detail, the joints incorporate a tension-amplification-tendon mechanism, significantly enhancing overall stiffness and torque. The links are optimized using finite element topology and lattice optimization techniques, mimicking the radially graded structure found in bone. This bio-inspired design effectively reduces weight and inertia while maximizing structural rigidity. To ensure consistent performance, we have also developed a novel pretension mechanism that allows for adjustable cable tension, preventing unwanted cable relaxation. Experimental validation demonstrates that the ATOM can achieve high-stiffness and high-torque with minimal CPD while exhibiting robust waterproof performance, showcasing its potential for advanced air-ground collaborative tasks.**

***Index Terms*—Aerial systems: mechanics and control, aerial robots, coupling disturbance, tendon-driven manipulator.**

I. Introduction

Aerial manipulator systems (AMSs) have been increasingly employed in tasks that pose risks or challenges to humans, such as aerial grasping [1], aerial manipulation [2], [3], contact inspection [4], and environmental monitoring [5]. One of the primary challenges in AMS flight control is addressing coupling disturbance (CPD) [6], which is caused by manipulator motions and represents a major source of lumped disturbances [7]. Current research often compensates for CPD using disturbance estimation techniques, such as various forms of observers [8], [9]. Alternatively, when a CPD model is accurately established based on variable-inertia-parameters, feedforward compensation provides a more direct and rapid approach to disturbance rejection [6], [7]. For example, [7] implements a CPD-feedforward PID on an AMS with an 4-DOF OpenManipulator (arm $0.702\,\mathrm{kg}$; total $3.35\,\mathrm{kg}$): during manipulator swing with a period of $20\,\mathrm{s}$, the maximum absolute hover-position error drops from $364\,\mathrm{mm}$ to $107\,\mathrm{mm}$ versus a conventional PID. Likewise, [6] applies a CPD-feedforward robust H_∞ controller to an AMS with a 2-DOF arm ($0.69\,\mathrm{kg}$; total $3.69\,\mathrm{kg}$); under comparable conditions (swing period $\approx 12\,\mathrm{s}$), the mean absolute position error is $47\,\mathrm{mm}$ in x-direction and $43\,\mathrm{mm}$ in y-direction.

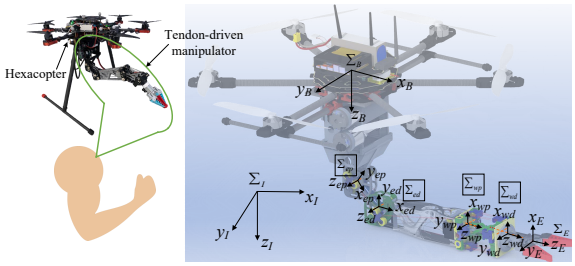

Fig. 1. The proposed ATOM and its coordinate frames. A Supplementary Video is available at https://youtu.be/AqUWnYyCHKw.

In practice, even for desktop-level robotic arms deployed on AMSs, the effectiveness of the CPD suppression has a significant impact on controller performance. For industrial arms with superior performance, CPD can further compromise system stability and safety. In study [10], the KUKA LWR was innovatively mounted on a helicopter for aerial manipulation. However, the strong CPD due to manipulator motion required exploiting the redundant DOF of the arm to mitigate divergent low-frequency attitude oscillations of the aircraft. It is worth noting that when AMSs are equipped with low-mass, low-inertia manipulators, CPD are relatively minor compared to external disturbances, rendering their effects negligible [11]. Nonetheless, overly lightweight manipulators generally exhibit low stiffness, resulting in limited operational performance [7]. Therefore, the trade-off between mitigating CPD and maintaining manipulator performance imposes a substantial constraint on the development of AMSs. To address these limitations while alleviating the control challenges introduced by CPD, this letter proposes a novel AMS prototype designed to achieve an optimal balance between reducing CPD and enhancing both stiffness and joint torque.

In the case where the motion commands for the UAV and

Manuscript received: Sep. 05, 2025; Accepted Nov. 01, 2025. This paper was recommended for publication by Editor Gosselin, Clement upon evaluation of the Associate Editor and Reviewers' comments.

This work was supported partially by the National Natural Science Foundation of China (Grant No. 62273122), Heilongjiang Natural Science Foundation (Grant No. YQ2023F009), and open research fund of Anhui Provincial Key Laboratory of Intelligent Low-Carbon Information Technology and Equipment. (Corresponding author: Zhan Li.)

Zhan Li, Quman Xu and Yipeng Yang are with the Research Institute of Intelligent Control and Systems, Harbin Institute of Technology, Harbin 150001, China (e-mail: zhanli@hit.edu.cn; 21b904024@stu.hit.edu.cn; ypyang@hit.edu.cn). Hai Li is with the Institute of Systems Engineering, China Academy of Engineering Physics, Mianyang 621999, China.(e-mail: lihai904011@caep.cn). Xinghu Yu is with the Ningbo Institute of Intelligent Equipment Technology Comapany Ltd., Ningbo 315201, China (e-mail: yuxinghu1012@126.com). Zhang Chen is with the Department of Automation, Tsinghua University, Beijing 100084, China (e-mail: cz_da@tsinghua.edu.cn).

manipulator are predefined, by analyzing the CPD model in [6], it is evident that CPD is caused by the movements of the manipulator's center of mass (COM) and changes in its inertia. Traditional serial manipulators exacerbate this issue due to their dispersed components, particularly the relatively heavy actuators at the joints [10], [12]. To address this challenge, [13] suggests placing the actuators as close as possible to the base of the high-altitude platform, thereby mitigating CPD in AMS. From this perspective, the work in [14] adopts timing belt transmission to realize a compact AMS, achieving low CPD and reduced inertia. This design also minimizes static unbalance in the AMS [15]. However, this design's scalability proves limited for multi-DOF manipulator applications. Alternatively, parallel mechanisms offer a promising approach [16], yet they generally come with the drawback of a constrained operational workspace compared to serial manipulators [13]. Based on this discussion, tendon-driven serial manipulators (TDSMs) present an excellent choice. TDSMs centralize the mechatronic servo system at the base, utilizing cables to remotely drive joint movements [17]. This design significantly reduces the weight and size of the joints while improving waterproofing and dustproofing capabilities, thereby enhancing safety during interactions [18]. In [17], the lightweight BioRob manipulator with spring-pretension tendon-driven actuation was developed , achieving safe physical human-robot interaction while achieving a payload capacity of up to 2 kg. Furthermore, TDSMs can achieve exceptional performance via complex designs [19]. Kim developed a movable-pulley-based tension amplification mechanism, successfully implementing it in both 1-DOF and 2-DOF joint configurations to create the advanced LIMS-AMBIDEX [20], [21]—a high-performance TDSM that combines low inertia with industrial-grade stiffness. Although existing studies on TDSMs primarily focus on ground-based collaborative robotic arms, their advantages and potential for AMS platforms remain highly promising.

Nevertheless, several critical challenges must be addressed during integrating TDSMs into AMS. First, the high-frequency vibrations during flight subject tendons to periodic stress, necessitating the development of a robust pretension mechanism to prevent tendon deformation and relaxation. Simultaneously, tension regulation proves to be an effective means of resonance suppression. This also means that BioRob's spring-pretension method is not applicable on AMS. Second, current research AMSs predominantly use small desktop-class arms or single-link arms [2]–[4], [6]–[9], [11] , since larger arms introduce severe CPD. Even high-performance arms like LIMS require thorough optimization in design and material selection to achieve the necessary weight reduction while maintaining critical stiffness and strength - the essential prerequisites for a flight-worthy low-CPD AMS.

Based on the above discussion, this work proposes a novel aerial tendon-driven manipulator (ATOM). ATOM features a higher stiffness manipulator and reduced CPD (see Fig. 1). The ATOM integrates a hexacopter (650 mm wheelbase) with a 4-DOF TDSM, which consists of a 1-DOF elbow joint and a 3-DOF wrist joint, mimicking the structure of a human arm. Our design addresses pretension and weight reduction; additionally, actuators are positioned on a base fixed to the UAV. The ATOM has a total weight of approximately 6.8 kg, with the movable portion of the arm accounting for only 0.966 kg. The main contributions of this letter are :

- A new design concept has been proposed based on an analysis of the CPD model, leading to the development of a novel TDSM for AMS. In this design, all electromechanical servo systems are located at the base, which effectively mitigates excessive CPD within the AMS. Additionally, the use of tendons provides the joints with high stiffness and torque. This combination expands new ideas for prototype design of AMS.
- Detailed structural design and optimization of the manipulator, including the development of lightweight pretension mechanisms with adjustable tension, incorporates finite element topology and lattice optimization techniques that mimic the radially graded structure found in bone. These techniques achieve weight reduction while maintaining high stiffness and strength.

The remainder of this paper is organized as follows: Section II derives the dynamic and the CPD model of the AMS. Section III describes the mechanical design, structural analysis, weight reduction, and overall configuration of the manipulator. Section IV presents the experimental results, and Section V concludes the paper by summarizing the key findings.

TABLE I
NOMENCLATURE

Symbol	Description
Σ_I, Σ_B	Inertial frame; body-fixed frame at UAV COM
${}^I\boldsymbol{R}_B$, ${}^B\boldsymbol{R}_I$	Rotations $\Sigma_B \to \Sigma_I$ and $\Sigma_I \to \Sigma_B$ $(= {}^I\boldsymbol{R}_B^{-1})$
$\boldsymbol{g}$, Φ	Gravity vector; Euler angles $[\phi, \theta, \psi]^\top$
${}^I\boldsymbol{P}_B$, ${}^I\dot{\boldsymbol{P}}_B$, ${}^I\ddot{\boldsymbol{P}}_B$	UAV COM position, velocity, and acceleration in Σ_I
${}^B\boldsymbol{\omega}_B$, ${}^B\dot{\boldsymbol{\omega}}_B$	UAV angular velocity and acceleration in Σ_B
${}^I\boldsymbol{f}$, ${}^I\boldsymbol{f}_c$	Thrust and CPD force in Σ_I
${}^B\boldsymbol{\tau}$, ${}^B\boldsymbol{\tau}_c$	Propeller and CPD torque in Σ_B
m_A, m_U, m_M	Total, UAV, and manipulator masses
${}^B\boldsymbol{r}_{om}$, ${}^B\dot{\boldsymbol{r}}_{om}$, ${}^B\ddot{\boldsymbol{r}}_{om}$	Manipulator COM and its first/second time derivatives in Σ_B
${}^B\boldsymbol{I}_M$, ${}^B\dot{\boldsymbol{I}}_M$	Manipulator inertia and its time derivative in Σ_B
m_{Li}, m_{Mi}	Masses of the i-th link and actuator
${}^B\boldsymbol{p}_{cLi}$, ${}^B\boldsymbol{p}_{cMi}$	COM positions of the i-th link and actuator in Σ_B
${}^B\boldsymbol{R}_{Li}$, ${}^B\boldsymbol{R}_{Mi}$	Rotations from link/actuator COM frames to Σ_B
$\boldsymbol{I}_{Li}^{\Sigma_{Li}}$, $\boldsymbol{I}_{Mi}^{\Sigma_{Mi}}$	Inertia tensors of link/actuator in their COM frames
n	Number of link–actuator groups
$[\cdot]_\times$	Skew-symmetric operator

II. Dynamics and CPD Model

The coordinate frames follow Fig. 1, and key symbols are summarized in Table I. The AMS translational and rotational dynamics are

$$ {}^I\ddot{\boldsymbol{P}}_B = \boldsymbol{g} + ({}^I\boldsymbol{f} + {}^I\boldsymbol{f}_c)/m_A \tag{1} $$

$$ {}^B\dot{\boldsymbol{\omega}}_B = {}^B\boldsymbol{I}_U^{-1}\left({}^B\boldsymbol{\tau} - [{}^B\boldsymbol{\omega}_B]_\times {}^B\boldsymbol{I}_U {}^B\boldsymbol{\omega}_B + {}^B\boldsymbol{\tau}_c\right) \tag{2} $$

The CPD wrench $({}^I\boldsymbol{f}_c,\ {}^B\boldsymbol{\tau}_c)$ follows the variable inertia parameters model [7]:

$$
\begin{aligned}
{}^I\boldsymbol{f}_c &= -m_M {}^I\boldsymbol{R}_B\left([{}^B\boldsymbol{\omega}_B]_\times^2 {}^B\boldsymbol{r}_{om} + {}^B\dot{\boldsymbol{\omega}}_B \times {}^B\boldsymbol{r}_{om} + 2[{}^B\boldsymbol{\omega}_B]_\times {}^B\dot{\boldsymbol{r}}_{om}\right), \\
{}^B\boldsymbol{\tau}_c &= -{}^B\boldsymbol{I}_M {}^B\dot{\boldsymbol{\omega}}_B - [{}^B\boldsymbol{\omega}_B]_\times \left({}^B\boldsymbol{I}_M {}^B\boldsymbol{\omega}_B\right) - {}^B\dot{\boldsymbol{I}}_M {}^B\boldsymbol{\omega}_B \\
&\quad + m_A\left({}^B\boldsymbol{r}_{om} \times {}^B\boldsymbol{R}_I(\boldsymbol{g} - {}^I\ddot{\boldsymbol{P}}_B) + {}^B\ddot{\boldsymbol{r}}_{om} \times {}^I\boldsymbol{R}_B {}^I\dot{\boldsymbol{P}}_B\right) \\
&\quad - \frac{m_A^2}{m_M}\left({}^B\boldsymbol{r}_{om} \times {}^B\ddot{\boldsymbol{r}}_{om} + {}^I\boldsymbol{R}_B {}^I\dot{\boldsymbol{P}}_B \times ([{}^B\boldsymbol{\omega}_B]_\times {}^B\dot{\boldsymbol{r}}_{om}) \right. \\
&\quad \left. + [{}^B\boldsymbol{\omega}_B]_\times ({}^B\boldsymbol{r}_{om} \times {}^B\dot{\boldsymbol{r}}_{om}) + {}^I\boldsymbol{R}_B {}^I\dot{\boldsymbol{P}}_B \times {}^B\dot{\boldsymbol{r}}_{om}\right),
\end{aligned} \tag{3}
$$

IEEE Robotics and Automation Letters (RA-L) paper, presented at ICRA 2026, Vienna, Austria. Cite as RA-L paper.

The aggregate manipulator COM and inertia in Σ_B are:

$$
\begin{aligned}
{}^B\boldsymbol{r}_{om} &= \frac{1}{m_A}\sum_{i=1}^{n}(m_{Li}{}^B\boldsymbol{p}_{cLi} + m_{Mi}{}^B\boldsymbol{p}_{cMi}),\\
{}^B\boldsymbol{I}_M &= \sum_{i=1}^{n}\Big({}^B\boldsymbol{R}_{Li}\boldsymbol{I}_{Li}^{\Sigma_{Li}}{}^B\boldsymbol{R}_{Li}^{-1} + {}^B\boldsymbol{R}_{Mi}\boldsymbol{I}_{Mi}^{\Sigma_{Mi}}{}^B\boldsymbol{R}_{Mi}^{-1}\\
&\quad + m_{Li}(\left\|{}^B\boldsymbol{p}_{cLi}\right\|^2\boldsymbol{I}_{3\times3} - {}^B\boldsymbol{p}_{cLi}{}^B\boldsymbol{p}_{cLi}^T)\\
&\quad + m_{Mi}(\left\|{}^B\boldsymbol{p}_{cMi}\right\|^2\boldsymbol{I}_{3\times3} - {}^B\boldsymbol{p}_{cMi}{}^B\boldsymbol{p}_{cMi}^T)\Big),
\end{aligned}
\tag{4}
$$

Remark 1: The movement of the manipulator changes ${}^B\boldsymbol{r}_{om}$ and ${}^B\boldsymbol{I}_M$ dynamically, increasing the resultant CPD. Placing the actuators on a fixed base significantly reduces these terms in (4), minimizing CPD during operation. In contrast, traditional manipulators with joint-mounted actuators result in larger values for ${}^B\boldsymbol{p}_{cMi}$, significantly increasing the CPD due to the relatively large mass and inertia of the actuators within the manipulator.

III. Mechanical Design of the Manipulator

A. Design of Joints

1) Analysis of Human Arm Joint: Inspired by human anatomy [22], the human elbow functions as a 1-DOF rotational joint primarily controlled by the antagonistic actions of the biceps brachii and triceps brachii. The wrist joint enables multiple movements, including: forearm pronation and supination driven by the pronator teres and supinator muscles, respectively; wrist flexion controlled by the flexor carpi radialis and extension by the extensor carpi radialis; radial deviation initiated by the flexor carpi radialis and ulnar deviation by the flexor carpi ulnaris. Each joint movement can be replicated using a set of mutually antagonistic tendons. To achieve smooth, dead-zone-free motion, the tendons must remain synchronized in real-time and maintain consistent tension, which forms a critical aspect of the design process.

2) Tension Amplification Tendon (TAT) Mechanism: The TAT mechanism consists of a cable guided through multiple movable pulleys. As shown in Fig. 2, when the motor applies a torque of τ_m, the total output pulling force of the tendon can be expressed as $T_{tat} = N \cdot \frac{\tau_m}{R_{cap}}$, where R_{cap} is the radius of the capstan, and N is the number of times the cable is wound around the movable pulleys. Using the principle of virtual work, the stiffness of the TAT can be derived as

$$
E_{tat} = \frac{T_{tat}}{\delta x_{tat}} = \frac{N \cdot T_c}{\delta x_c / N} = N^2 k_c. \tag{5}
$$

where δx_{tat} represents the deformation of the TAT, and T_c, δx_c, and k_c denote the tension, deformation, and stiffness of the cable, respectively. The TAT mechanism enhances the load-bearing capacity and stiffness of cable-driven systems and acts as a reducer at the joints.

3) Design and Kinematic Analysis of the Elbow Joint: The design details and a simplified model of the elbow joint are shown in Fig. 3. The motion of the elbow joint is achieved through pure rolling between circular surfaces (see Fig. 3(a)-(b)). Based on the geometric relationships illustrated in Fig. 3(c)-(f), when the elbow joint rotates by an angle θ, with a curvature radius R and a distance d_e between the

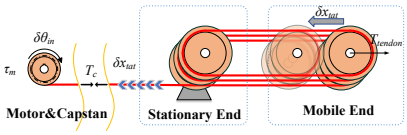

Fig. 2. TAT mechanism based on the principle of the movable pulley.

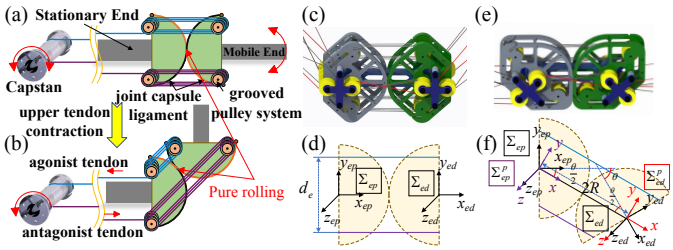

Fig. 3. Elbow Joint Utilizing TAT. (a) Initial state. (b) Bending state. (c) 1-DOF joint (initial state). (d) Schematic diagram of the 1-DOF joint (initial state). (e) 1-DOF joint (bending state). (f) Schematic diagram of the 1-DOF joint (bending state).

agonist TAT (AGT) and the antagonist TAT (ANT), the lengths of the AGT and the ANT can be expressed as

$$
L_{agt} = N_e(2R - d_e\sin(\theta/2)), \quad L_{ant} = N_e(2R + d_e\sin(\theta/2)), \tag{6}
$$

where N_e is the number of windings of the TAT. From (6), the changes in length of the AGT and ANT are given by

$$
\Delta L_{agt} = -N_e d_e \sin(\theta/2), \quad \Delta L_{ant} = N_e d_e \sin(\theta/2). \tag{7}
$$

This ensures that pure rolling maintains symmetrical TAT motion. To achieve stability and prevent slippage during pure rolling, a mechanism analogous to a joint capsule is implemented. This is accomplished using two sets of intersecting cables, which not only maintain pure rolling but also enhance the torsional rigidity of the elbow joint (see Fig. 3(a)-(d)). This symmetrical configuration allows both AGT and ANT to wind around a single capstan, which is driven by one actuator.

Coordinate systems are established at the center of the fixed end and the center of the moving end of the elbow joint, denoted as $\Sigma_{ep}\{O_{ep}-X_{ep}Y_{ep}Z_{ep}\}$ and $\Sigma_{ed}\{O_{ed}-X_{ed}Y_{ed}Z_{ed}\}$, respectively. To facilitate the description of the homogeneous transformations between Σ_{ep} and Σ_{ed}, intermediate coordinate systems Σ_{ep}^p and Σ_{ed}^p are introduced, where the transformation sequence is described as $\Sigma_{ep} \to \Sigma_{ep}^p \to \Sigma_{ed}^p \to \Sigma_{ed}$. The axes of each coordinate system are color-coded for clarity. The homogeneous transformation between Σ_{ep} and Σ_{ed} is expressed as ${}^{ep}\boldsymbol{T}_{ed} = Rot(Z,\theta/2)\,Trans(X,2R)\,Rot(Z,\theta/2)$.

4) Design and Kinematic Analysis of Wrist Joint: The design details and a simplified model of the wrist joint are shown in Fig. 4. The wrist joint has a 2-DOF parallel mechanism for wrist flexion-extension (pitch) and ulnar-radial deviation (yaw), combined with a serial 1-DOF joint for forearm pronation and supination (roll) (Fig. 4(a)–(c)).

The 2-DOF joint leverages a parallel mechanism based on an antiparallelogram linkage. Similar to the elbow joint, symmetrical TAT motion is achieved during pure rolling on a spherical surface. For planar motion, the antiparallelogram linkage generates rolling motion between two designable ellipses, approximating pure rolling between circular surfaces. The fundamental principle is illustrated in Fig. 5.

IEEE Robotics and Automation Letters (RA-L) paper, presented at ICRA 2026, Vienna, Austria. Cite as RA-L paper.

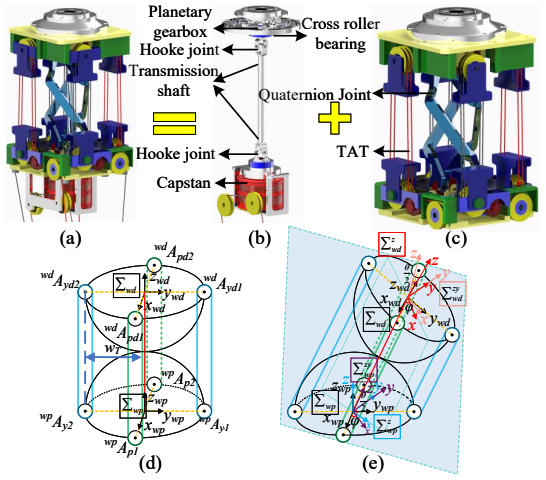

Fig. 4. Detail design of the wrist joint. (a) 3-DOF wrist joint. (b) 1-DOF joint. (c) 2-DOF joint. (d) Schematic diagram of the 2-DOF joint (initial state). (e) Schematic diagram of the 2-DOF joint (bending state).

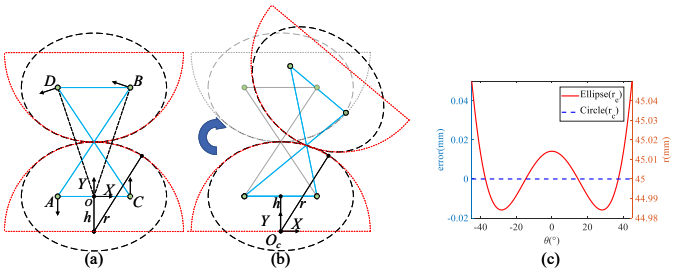

Fig. 5. Anti-parallelogram mechanism. (a) Initial state. (b) Approximation between circular rolling motion and elliptical rolling motion. (c) Error curve between the ellipse and the approximated circle.

Clearly, the antiparallelogram mechanism functions as a 1-DOF revolute joint. From Fig. 5(a), when the link lengths are defined as AB = CD = l and AC = BD = $2w$, the trajectory of the intersection point P forms an ellipse $\frac{x^2}{(l/2)^2}+\frac{(y-h)^2}{(l/2)^2-w^2}=1$.

By selecting appropriate parameters, the elliptical arc over a specific motion range can approximate a circular arc. To quantify the approximation error, a polar coordinate system O_{C-XY} is established at the center of the desired circle (see Fig. 5(b)), where the ellipse's polar radius is given by

$$r_e=\frac{h\cos(\theta)+\sqrt{h^2\cos^2(\theta)-4\left(\frac{\cos^2(\theta)}{l^2-4w^2}+\frac{\sin^2(\theta)}{l^2}\right)\left(\frac{4h^2}{l^2-4w^2}-1\right)}}{4\left(\frac{\cos^2(\theta)}{l^2-4w^2}+\frac{\sin^2(\theta)}{l^2}\right)}.$$

To approximate a circular segment with radius r_c over the range $-\pi/4 < \theta < \pi/4$, the following constrained optimization problem is constructed:

$$\min_{h,l}\left(\int_{-\frac{\pi}{4}}^{\frac{\pi}{4}}|r_e(\theta)-r_c(\theta)|d\theta\right),\quad s.t\quad r_c(\theta)=40, w=12. \tag{8}$$

Using $h = 3.43$ mm and $l = 76.95$ mm, the fitting error across the entire motion range is minimized to less than 0.05 mm, as shown in Fig. 5(c). This configuration achieves a rotation range of $[-\pi/2, \pi/2]$.

The planar 1-DOF antiparallelogram mechanism can be extended to a 2-DOF configuration with three branches [21], [23]. The intersection points of the linkages lie on an ellipsoidal surface $\frac{x^2}{(l/2)^2}+\frac{(y-h)^2}{(l/2)^2-w^2}+\frac{z^2}{(l/2)^2}=1$. As shown in Fig. 4(d–e), the branches are evenly distributed at 120° intervals, with two rotational pairs added to both the moving and stationary platforms. Theoretically, this configuration is fully constrained. However, due to minor deformations in the linkages under slight stress or machining errors , the mechanism can tilt in two directions. A more in-depth discussion of such 3-UU mechanisms can be found in [24]. Fig. 4(d–e) illustrates the schematic diagram of the 2-DOF wrist joint. The base coordinate system Σ_{wp} is established at the center of the proximal end, while the distal end of the wrist joint serves as the moving coordinate system Σ_{wd}. Similar to Section III-A3, intermediate coordinate systems ($\sum_{wp} \rightarrow \sum_{wp}^{r} \rightarrow \sum_{wp}^{rp} \rightarrow \sum_{wd}^{rp} \rightarrow \sum_{wd}^{r} \rightarrow \sum_{wd}$) are introduced to simplify the description of homogeneous transformations between Σ_{wp} and Σ_{wd}. Colored bounding boxes are added to the frames of these intermediate coordinate systems, corresponding to the axes of their respective coordinate systems. Assuming the tendon is positioned at a distance w from the center of the wrist, and considering the bending direction ϕ and bending angle θ, the motion of the 2-DOF part of the wrist joint can be simplified as pure rolling on a plane inclined at an angle ϕ to the XOZ plane of the wrist joint's proximal coordinate system. The homogeneous transformation matrix from the distal to the proximal end of the 2-DOF section, denoted as ${}^{wp}\boldsymbol{T}_{wd} \in SE(3)$, is ${}^{wp}\boldsymbol{T}_{wd} = Rot(Z,\phi)Rot(Y,\theta/2)Trans(Z,h)Rot(Y,\theta/2)Rot(Z,-\phi)$.

The changes in TAT lengths can be calculated as

$$\begin{aligned} L_{p_1}&=\left|{}^{wp}\boldsymbol{A}_{p_1}-{}^{wp}\boldsymbol{T}_{wd}\,{}^{wd}\boldsymbol{A}_{pd_1}\right|, L_{p_2}=\left|{}^{wp}\boldsymbol{A}_{p_2}-{}^{wp}\boldsymbol{T}_{wd}\,{}^{wd}\boldsymbol{A}_{pd_2}\right|,\\ L_{y_1}&=\left|{}^{wp}\boldsymbol{A}_{y_1}-{}^{wp}\boldsymbol{T}_{wd}\,{}^{wd}\boldsymbol{A}_{yd_1}\right|, L_{y_2}=\left|{}^{wp}\boldsymbol{A}_{y_2}-{}^{wp}\boldsymbol{T}_{wd}\,{}^{wd}\boldsymbol{A}_{yd_2}\right|, \end{aligned}$$

where L_{p_1}, L_{p_2}, L_{y_1}, and L_{y_2} correspond to the tendon lengths in the pitch and yaw directions, respectively. The homogeneous coordinates of the tendon endpoints are defined as ${}^{wp}\boldsymbol{A}_{p_1} = {}^{wd}\boldsymbol{A}_{pd_1} = (w,0,0,1)$; ${}^{wp}\boldsymbol{A}_{p_2} = {}^{wd}\boldsymbol{A}_{pd_2} = (-w,0,0,1)$; ${}^{wp}\boldsymbol{A}_{y_1} = {}^{wd}\boldsymbol{A}_{yd_1} = (0,w,0,1)$; ${}^{wp}\boldsymbol{A}_{y_2} = {}^{wd}\boldsymbol{A}_{yd_2} = (0,-w,0,1)$. For each pair of mutually antagonistic TATs, the length changes of the AGTs and ANTs are symmetrical. The total change in tendon lengths can be expressed as

$$\begin{aligned} \Delta L_{pitch} &= 2N_w w\cos(\varphi)\sin(\theta/2),\\ \Delta L_{yaw} &= 2N_w w\sin(\varphi)\sin(\theta/2), \end{aligned} \tag{9}$$

where N_w represents the number of windings of the TAT's cable in the 2-DOF joint.

As shown in Fig. 4(b), to avoid coupling with the 2-DOF TATs, the 1-DOF joint for wrist pronation and supination is driven independently by a capstan mechanism. The driving tendon is routed through the forearm, proximal to the 2-DOF joint. The capstan rotates under the traction of an actuator at the manipulator's base, with its motion transmitted to the wrist via a transmission shaft. The transmission shaft passes through two Hooke's joints arranged in series, accommodating the wrist's rolling motion while maintaining effective torque transfer. A planetary gearbox at the wrist's distal end amplifies the output torque and stiffness. The kinematic relationship of this joint can be determined based on the capstan diameter and the reducer's reduction ratio.

IEEE Robotics and Automation Letters (RA-L) paper, presented at ICRA 2026, Vienna, Austria. Cite as RA-L paper.

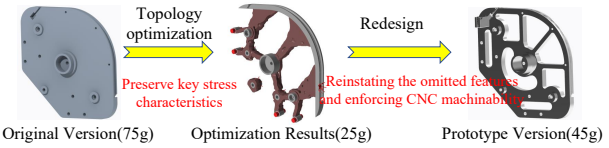

Fig. 6. Finite element-based weight reduction of elbow joint.

B. Torque and Stiffness Analysis of Joints

1) Analysis of the Elbow Joint: From Fig. 3, the torque of the elbow joint can be expressed as $\tau_{elb}\Delta\theta = \Delta T \Delta l$, where $\Delta\theta$ represents the joint rotation angle, ΔT is the tension difference in a single cable between the AGT and ANT, and Δl denotes the displacement of the tendon cable.

Considering the symmetry of the AGT and ANT, and using (6), the following relationship is obtained:

$$\frac{\Delta l}{\Delta\theta} = \frac{N_e d_e}{2}\cos(\theta/2). \tag{10}$$

The output torque of the joint can be deduced as

$$\tau_{elb} = \frac{N_e d_e}{2}\cos(\theta/2)\Delta T. \tag{11}$$

Assuming the joint is in equilibrium at an angle θ, and an external torque δ_τ is applied, the joint undergoes a small angular deformation δ_θ. According to the principle of virtual work, the following equation is obtained:

$$\delta\tau\delta\theta = \Sigma_{i=1}^{N_e}\delta T_i \delta L_i. \tag{12}$$

By combining (10) and (12), it can be deduced that

$$\delta\tau = \frac{N_e d_e}{2}\cos(\theta/2)(T_{agt} - T_{ant}) = \frac{N_e d_e}{2}\cos(\theta/2)k_c 2\delta l. \tag{13}$$

The stiffness of the elbow joint can be derived as

$$k_{elb} = \frac{\delta\tau}{\delta\theta} = \frac{(N_e d_e \cos(\theta/2))^2}{2}k_c. \tag{14}$$

2) Analysis of the Wrist Joints: The torque and stiffness for the 2-DOF portion of the wrist joint can be calculated using (9) and the analysis in Section (III-B1). The resultant output torque and stiffness for a single pair of antagonistic TATs are similarly derived. When both tendons are engaged, the total output torque for the 2-DOF section is given by

$$\tau_{2dof} = N_w w_T \cos(\theta/2)\left(\Delta T_{pitch}\,|\cos(\varphi)| + \Delta T_{yaw}\,|\sin(\varphi)|\right), \tag{15}$$

here, w_T refers to the distance from the TATs to the center (see Fig. 4). Similarly, the joint stiffness for the 2-DOF portion when both tendons are engaged can be calculated as

$$\begin{aligned} k_{2dof} &= \frac{1}{2}[(2N_w w_T \cos(\theta/2)\cos(\varphi))^2 + (2N_w w_T \cos(\theta/2)\sin(\varphi))^2]k_c \\ &= 2N_w^2 w_T^2 \cos^2(\theta/2)k_c \end{aligned} \tag{16}$$

A capstan with a radius of R_{cap}^{roll} is used to control the motion of the wrist joint in the roll direction. The output torque and stiffness in this direction, based on the planetary gear reducer with a gear ratio N_r, can be expressed as

$$\tau_{\text{roll}} = N_r R_{cap}^{\text{roll}}\Delta T, k_{\text{roll}} = 2\left(N_r R_{cap}^{\text{roll}}\right)^2 k_c. \tag{17}$$

Remark 2: From (11) and (14), increasing the design parameters N_e and d_e raises the elbow joint torque and stiffness. Equations (15)–(17) likewise show that larger N_w and w_T increase the output torque and stiffness of the 2-DOF wrist, while a higher gear ratio N_r and a larger R_{cap}^{roll} further improve performance in the roll direction. For a conventional cable–roller drive, setting $N_r = 1$ recovers the corresponding torque and stiffness expressions, as in (17).

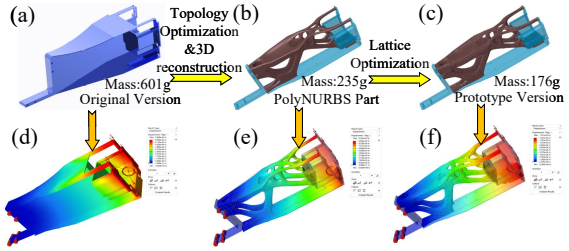

Fig. 7. Finite element-based weight reduction of elbow link. (a)–(c) depict the optimization steps. (d)–(f) present the finite element stiffness analysis under extreme impacts, such as AMS falls. Simulated conditions included a shear force of 500 N and a bending moment of 15 N·m applied at the distal end.

C. Topology Optimization for Weight Reduction

In aerial manipulation tasks, the manipulator components must be lightweight while maintaining high stiffness and strength. To meet these requirements, topology optimization (TO) was performed for the heavier components of the manipulator. Boundary conditions were established based on operational constraints and applied forces, and the optimization process was conducted using *Altair Inspire 2022*.

Considering the TAT system setup and pulley requirements for cable routing at each joint, post-optimization redesigns were implemented based on the TO results, as shown in Fig. 6. Through optimization, the weight of the elbow joint was reduced by 40% compared to its original design.

Beyond the fixed tendon sheath structure for the end-effector's motion path, the manipulator links primarily require space for joint installation. To enhance optimization outcomes, the initial design space was expanded while ensuring no interference with the tendon paths. After defining the design space, TO was performed to maximize stiffness under various load conditions involving bending and torsional deformations. The mass target was set to 30% of the total design space volume. Subsequently, lattice optimization was applied to the links, mimicking the radially gradient structure of human bone. This approach aimed to reduce weight and inertia while maximizing stiffness under AMS operating conditions. Lattice parameters were set with a target strut length of 6 mm and diameters ranging from 1 mm to 2 mm, filling the available design space. The optimization process is illustrated in Fig. 7. The optimization process achieved a total weight reduction of 71% for the manipulator link, considering both optimized and non-optimized assembly areas. Within the optimized regions specifically, the weight was reduced by 83%. Finite element stiffness calculations showed only a 2.4-fold decrease in stiffness, with no evidence of plastic deformation under impact loads, indicating sufficient residual strength.

D. Overall Configuration of the ATOM

To better validate the CPD characteristics, we selected a hexacopter with a 650mm diagonal motor-to-motor distance—intermediate between the 550mm platform in [7] and

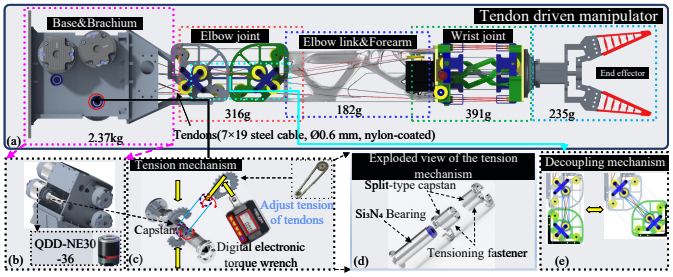

Fig. 8. TDSM CAD model. (a) Manipulator schematic; (b) Upper arm, comprising the tensioning mechanism and actuators. QDD-NE30-36 denotes a robot joint module with a multi-turn absolute encoder and a 36:1 reduction; given the safety requirements of AMS, integrated joint modules are a preferable choice for tendon actuation; (c) Tensioning mechanism and its tensioning process; (d) Exploded view of the tensioning mechanism, similar to the actuation unit of the da Vinci surgical robot; (e) Decoupling mechanism.

the 800mm platform in [6]—as the flight platform. The overall hardware setup is shown in Fig.12, and Fig. 8 details the manipulator's structure and key components. The TDSM actuators are mounted on the UAV-attached base, ensuring synchronized length changes of the AGTs and ANTs during joint motion. A decoupling pulley at the elbow mechanically isolates the elbow and wrist motions (Fig. 8(e)).

Mechanical pretension of each tendon is essential for maintaining motion accuracy under load and enabling quick reverse movements. Given the weight sensitivity of the AMS, the pretension mechanism's weight and size are critical. Although both rotating screw and ratchet mechanisms at the cable end are lightweight, they present challenges in force control and smoothness, respectively. In this design, each capstan assembly comprises a rotating shaft together with AGT and ANT capstans (Figs. 8(b)–(d)). The rotating shafts are connected to the actuators, and the pretension for both the AGT and ANT capstans can be precisely adjusted via sprocket systems and torque capstans. The pretension force is set to half of the steel cable's maximum load.

The primary structure of the TDSM must possess high strength and stiffness to withstand substantial forces and torques. Therefore, 7075 aluminum alloy is used for the main structural components. Additionally, AlSi10Mg, fabricated using selective laser melting, is employed for lattice-optimized forearm component, ensuring weight reduction without compromising mechanical properties. For components such as pulleys and gears, which transmit cable tension, durability and low friction are crucial. PEEK is chosen for these parts due to its superior wear resistance, stable chemical structure, low friction coefficient, and fatigue resistance.

IV. Experimental Analysis

A. TDSM Performance Validation

Before conducting flight tests on the ATOM, we first validated the TDSM for high stiffness, high torque, and waterproofing. Experiments covered three scenarios: (i) ground manipulation—moving heavy objects after the ATOM rapidly arrived and landed at a simulated disaster site; (ii) underwater grasping to verify basic grasping capability; and (iii) stiffness and limit-performance testing.

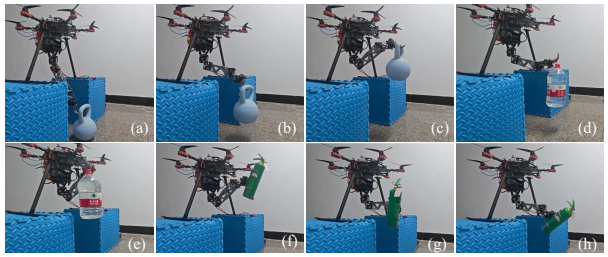

Fig. 9. Procedure and results for scenario (i). (a-c) Grasping the kettlebell. (d-e) Grasping the mineral water bottle. (f-h) Operating the fire extinguisher.

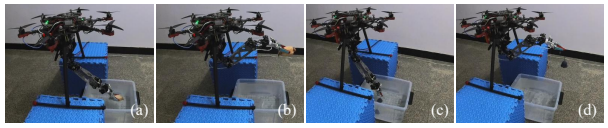

Fig. 10. Procedure and results for scenario (ii). (a-b) Grasping the lotus root. (c-d) Grasping the bell.

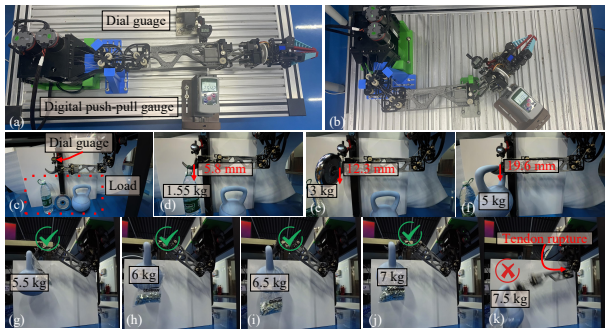

Fig. 11. Procedure and results for scenario (iii). (a–b) Experimental setup for joints stiffness measurement. (c–f) Setup and results for L_{TCP} measurement. (g–k) Setup and results for $L_{\max}$ measurement.

In scenario (i), ATOM was placed on two sponge-mat boxes while the TDSM manipulated heavy objects— a 5 kg kettlebell, 5 L bottled water, and a 2 kg fire extinguisher—using different end effectors. Snapshots are shown in Fig. 9 (additional views in the Supplementary Material). Enabled by its high stiffness and large joint torque, the TDSM reliably grasped and released a 5 kg load and reoriented the extinguisher, demonstrating ATOM's potential for ground operations in hard-to-access emergency settings (e.g., post-disaster response, assisted rescue, high-altitude platform firefighting).

In scenario (ii), the TDSM used a pneumatic, fin-shaped soft end effector (PFEE) actuated by an onboard air pump and valve mounted on the UAV. The setup mirrored scenario (i) but involved grasping two objects in a sink: a lotus root at the surface and a bell underwater. As shown in Figs. 10(a–d) (additional views in the Supplementary Material), the arm approached from above the water, adjusted the PFEE pose, closed the gripper, and lifted the objects out. These results show basic grasping and manipulation and, owing to the system's water-resistant design, indicate potential for underwater tasks—capabilities seldom reported in prior AMS work.

In scenario (iii), we evaluated four metrics: (a) k_{SE} and k_{SW}, the stiffness of the elbow and wrist joints; (b) L_{TCP}, the tool center point line stiffness under elbow flexion; and (c) $L_{\max}$, the maximum load during heavy-object grasping with elbow flexion. Joint stiffness was measured following

IEEE Robotics and Automation Letters (RA-L) paper, presented at ICRA 2026, Vienna, Austria. Cite as RA-L paper.

TABLE II
MEASURED STIFFNESS AND STRENGTH SPECIFICATIONS FOR TDSM.

Metric	k_{SE} (N · m/rad)			k_{SW} (N · m/rad)		L_{TCP} (N/m)	$L_{\max}$ (kg)
	0°	45°	90°	bending 0°	bending 45°	—	—
Value	737.8	666.2	478.8	254.7	220.6	2457.3	7

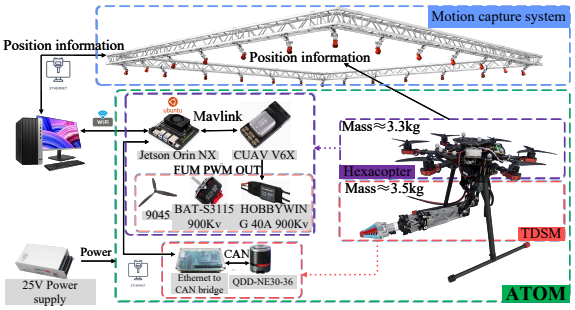

Fig. 12. Hardware of ATOM and experiment setup.

[20]. To obtain L_{TCP}, the TDSM base was rigidly fixed in the elbow-flexion pose and stepwise loads were applied at the end effector. To determine $L_{\max}$, we performed a grasping test analogous to scenario (i), increasing the load in steps until joint failure occurred. Figure 11 presents the setups and results (additional views in the Supplementary Material), and Table II reports the quantitative values. In our system, the maximum payload (∼7 kg) is governed by tendon tensile strength, whereas in LIMS [20] it is limited by motor/driver torque (∼3 kg). This difference arises from our use of thinner tendons and planetary-geared joint actuators (see Fig. 8), which makes the TAT the primary failure point ahead of the motors and drivers. A practical benefit is greater crash tolerance during early-stage testing : the TAT yields or fails before the motors and drivers, mitigating damage and lowering maintenance costs—at the expense of lower peak motion speed than LIMS. Despite the thinner tendons and a smaller TDSM (to meet UAV payload limits), the arm achieves strong stiffness for its size; for example, the maximum elbow stiffness is about one-half of that reported for LIMS. Overall, these trade-offs yield a compact arm for ATOM that is well suited to advancing AMS applications.

B. Low CPD Validation and In-flight Manipulation Test

After verifying the performance of TDSM, we demonstrate that our design effectively reduces the CPD of the AMS through a flight experiment. The hardware of ATOM and experiment setup are shown in Fig.12.

The experimental scenario for CPD validation begins with ATOM initially hovering at the position (0, 0, 1) m. After 10 s, the TDSM executes large-amplitude, rapid motions following a sinusoidal profile, starting with the elbow flexion at a right angle, extension to a straight configuration, and then returning to the right angle. Three different motion periods are employed for a more comprehensive investigation: case_1 at 10s, case_2 at 8s, and case_3 at 20/3s. The corresponding position response and position error are depicted in Fig.13, where it can be observed that, due to CPD, the X-direction exhibits the largest position deviation, reaching approximately 2.5mm in case_3. The multi-frame overlap image of the experiment for case_3 is

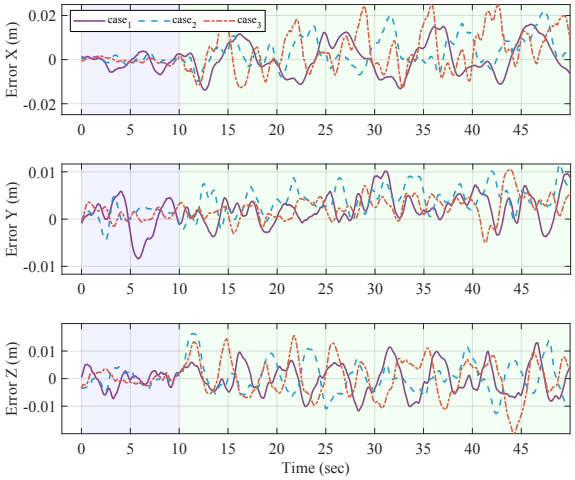

Fig. 13. State error of position in CPD validation indoor flight experiment. (A purple and green background are used to distinguish the hovering process and TDSM motion process, starting at 0s and 10s, respectively.)

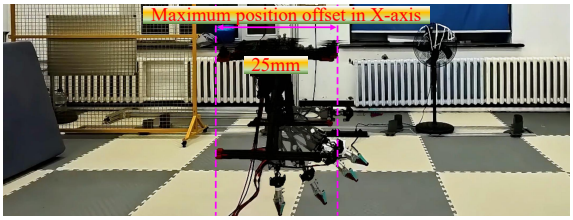

Fig. 14. Multi-frame overlap of CPD validation flight experiment.

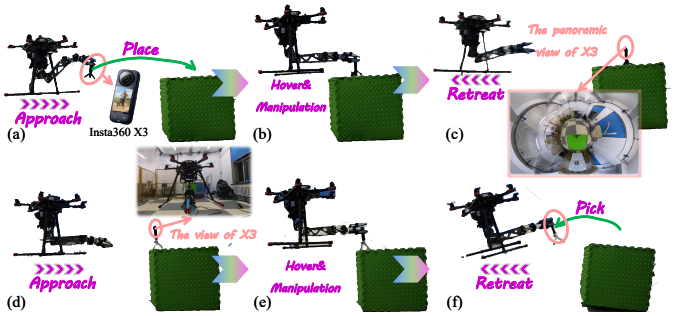

Fig. 15. The process of the in-flight placing and picking experiment. (a-c) Placing a panoramic action camera (simulating payloads such as surveillance devices or sensors) on a sponge mat box (simulating non-ground high-altitude platforms). (d-f) Picking the panoramic action camera from the sponge mat box.

shown in Fig.14 (see also the Supplementary Material). For quantitative analysis, statistical indicators—MEAN, MAX, and RMSE—are employed to evaluate position errors during both the hovering phase (0–10s) and the TDSM motion phase (10–50s). Since the operating conditions in the hovering phase are identical across all cases, the corresponding errors are aggregated for a unified statistical analysis, whereas the errors during the TDSM motion phase are evaluated separately for each case. The results are summarized in Table III. Taking the X-axis results from case_3 as an example, the maximum error increases from 4.3mm during hovering to 25mm during TDSM motion; the mean error rises from 1.6mm to 8.4mm, and the RMSE from 1.9m to 11mm. Although TDSM motion increases ATOM's hover error, the deviation remains within a very small range. Furthermore, compared with the experimental results reported in [6] and [7] (MAX along the X-

TABLE III
ANALYSIS OF EXPERIMENTAL ERRORS IN CPD VALIDATION.

Metric	Hovering Phase			Motion Phase (case$_1$)			Motion Phase (case$_2$)			Motion Phase (case$_3$)		
	X Axis	Y Axis	Z Axis	X Axis	Y Axis	Z Axis	X Axis	Y Axis	Z Axis	X Axis	Y Axis	Z Axis
MAX(mm)	4.3	5.6	5.2	16	10	13	22	13	16	25	11	20
MEAN(mm)	1.6	2.1	1.9	6.7	3.0	4.8	5.8	4.4	4.7	8.4	3.0	6.1
RMSE(mm)	1.9	2.5	2.4	8.0	3.8	5.6	7.8	5.1	6.0	11	3.6	7.2

axis: 107 mm [7]; MEAN along the X-axis: 47 mm [6]; see the review in Section I), it is evident that ATOM achieves substantially smaller hover errors during TDSM motion .

This observation is consistent with [11]. When a relatively low-mass, low-inertia manipulator is used for AMS (as stated in [11], where the arm is $\sim$0.6 kg and the UAV $\sim$3.5 kg), the CPD induced by arm motion is negligible. In our system, the moving subassembly is even lighter: the moving portion of the TDSM is only 0.966 kg, while the entire flight platform is $\sim$6.8 kg—an even smaller ratio than in [11]. Consequently, variations in arm motion have no discernible impact on the tracking error; their effect is subdominant to the lumped disturbance arising from model uncertainties and external disturbances. Additionally, we conduct pick-and-place experiments. In Scenario$_1$, ATOM places a 208g camera onto a sponge-mat box (see Fig.15(a–c)); in Scenario$_2$, ATOM retrieves the camera from the sponge-mat box and delivers it to the ground (see Fig. 15(d–f)). Detailed procedures are provided in the Supplementary Material.

Remark 3: The load capacity could be further increased by adopting thicker tendons and higher-torque joint modules.

Remark 4: The in-flight manipulation test further validates ATOM's basic in-flight manipulation capability. Together with its low-CPD characteristics and the high-torque TDSM that benefits contact-rich ground operations, ATOM shows strong potential for real-world air–ground cooperative tasks. That said, the manipulator on ATOM has substantially higher stiffness and torque than the desktop arms commonly used in current AMS studies; accordingly, future deployments should prioritize compliance control and carefully tuned transients to avoid overshoot-induced contact forces, which can undermine flight-control robustness [8].

V. CONCLUSION

This paper presents a novel AMS, ATOM, equipped with a 4-DOF anthropomorphic TDSM. The TDSM demonstrates excellent waterproof capabilities, as well as high-stiffness, high joint torque, and low-inertia, providing outstanding environmental adaptability and minimal CPD for ATOM. The total mass of ATOM is 6.8 kg, with the TDSM weighing 3.5 kg, and the moving part of the arm contributing only 0.966 kg. The design process includes the development of the elbow and wrist joints, a pretension structure, and the application of finite element topology and lattice optimization for weight reduction. Theoretical models were also developed to analyze joint torques and stiffness. The performance of ATOM was validated through underwater grasping experiments, heavy object manipulation, performance evaluation, low CPD validation, and in-flight manipulation test, and the results indicate the high output of the TDSM and the small CPD of ATOM. In future work, we plan to deploy ATOM for air-ground collaborative tasks in challenging environments and conduct further research on whole-body flight control algorithms based on task-specific requirements.

REFERENCES

[1] R. Peng, *et al.*, "A dexterous and compliant aerial continuum manipulator for cluttered and constrained environments," *Nat. Commun.*, vol. 16, no. 1, p. 889, Jan. 2025.
[2] A. González-Morgado, *et al.*, "How to shake trees with aerial manipulators? a theoretical and experimental study," *IEEE Rob. Autom. Lett.*, vol. 10, no. 8, pp. 8067–8074, Aug. 2025.
[3] G. He, *et al.*, "Flying Hand: End-Effector-Centric Framework for Versatile Aerial Manipulation Teleoperation and Policy Learning," in *Proc. Robotics, Sci. Syst.*, 2025.
[4] X. Guo, *et al.*, "Flying calligrapher: Contact-aware motion and force planning and control for aerial manipulation," *IEEE Robot. Automat. Lett.*, vol. 9, no. 12, pp. 11 194–11 201, Dec. 2024.
[5] W. R. Roderick, M. R. Cutkosky, and D. Lentink, "Bird-inspired dynamic grasping and perching in arboreal environments," *Sci. Rob.*, vol. 6, no. 61, p. Art. no. eabj7562, Dec. 2021.
[6] G. Zhang, *et al.*, "Robust control of an aerial manipulator based on a variable inertia parameters model," *IEEE Trans. Ind. Electron.*, vol. 67, no. 11, pp. 9515–9525, Nov. 2020.
[7] Z. Li, *et al.*, "Coupling disturbance modeling and compensation for aerial manipulator in highly dynamic motion," *IEEE Trans. Cybern.*, pp. 1–12, Jan. 2025.
[8] J. Byun, *et al.*, "A hybrid controller enhancing transient performance for an aerial manipulator extracting a wedged object," *IEEE Trans. Autom. Sci. Eng.*, vol. 21, no. 3, pp. 3264–3273, Jul. 2024.
[9] Y. Wu, *et al.*, "Learning variable whole-body control for agile aerial manipulation in strong winds," *IEEE Rob. Autom. Lett.*, vol. 10, no. 5, pp. 4794–4801, May 2025.
[10] F. Huber, *et al.*, "First analysis and experiments in aerial manipulation using fully actuated redundant robot arm," in *2013 IEEE/RSJ International Conference on Intelligent Robots and Systems*, 2013, pp. 3452–3457.
[11] Q. Liu, *et al.*, "A coordinated framework of aerial manipulator for safe and compliant physical interaction," *Control Eng. Pract.*, vol. 146, p. 105898, May. 2024.
[12] A. Mörtl, *et al.*, "The role of roles: Physical cooperation between humans and robots," *Int. J. Rob. Res.*, vol. 31, no. 13, pp. 1656–1674, Aug. 2012.
[13] A. Ollero, *et al.*, "Past, present, and future of aerial robotic manipulators," *IEEE Trans. Rob.*, vol. 38, no. 1, pp. 626–645, Feb. 2021.
[14] D. Wuthier, *et al.*, "On the design, modeling and control of a novel compact aerial manipulator," in *Proc. 24rd Mediterranean Conf. Control Automat.*, 2016, pp. 665–670.
[15] C. D. Bellicoso, *et al.*, "Design, modeling and control of a 5-DoF light-weight robot arm for aerial manipulation," in *in Proc. 23rd Mediterranean Conf. Control Automat.*, 2015, pp. 853–858.
[16] P. Chermprayong, *et al.*, "An integrated delta manipulator for aerial repair: A new aerial robotic system," *IEEE Rob. Autom. Mag.*, vol. 26, no. 1, pp. 54–66, Mar. 2019.
[17] T. Lens and O. von Stryk, "Investigation of safety in human-robot-interaction for a series elastic, tendon-driven robot arm," in *in Proc. IEEE/RSJ Int. Conf. Intell. Robots Syst.*, 2012, pp. 4309–4314.
[18] R. Ozawa, H. Kobayashi, and K. Hashirii, "Analysis, classification, and design of tendon-driven mechanisms," *IEEE Trans. Rob.*, vol. 30, no. 2, pp. 396–410, Apr. 2014.
[19] Y.-J. Kim, "Design of low inertia manipulator with high stiffness and strength using tension amplifying mechanisms," in *in Proc. IEEE/RSJ Int. Conf. Intell. Robots Syst.*, 2015, pp. 5850–5856.
[20] Y.-J. Kim, "Anthropomorphic low-inertia high-stiffness manipulator for high-speed safe interaction," *IEEE Trans. Rob.*, vol. 33, no. 6, pp. 1358–1374, Dec. 2017.
[21] Y.-J. Kim, J.-I. Kim, and W. Jang, "Quaternion joint: Dexterous 3-DOF joint representing quaternion motion for high-speed safe interaction," in *in Proc. IEEE/RSJ Int. Conf. Intell. Robots Syst.*, 2018, pp. 935–942.
[22] A. M. Agur and A. F. Dalley, *Grant's atlas of anatomy*. Lippincott Williams & Wilkins, 2009.
[23] K. Shikata, K. Masuya, and T. Sugihara, "Zero-DOF 3-UU parallel mechanism that inclines largely in two directions," in *in Proc. JSME Conf. Robot. Mechatronics*, 2014.
[24] G. Lang, *et al.*, "Kinematic analysis for the spatial interlocking 3-UU mechanism with the wide range of motion," *IEEE Rob. Autom. Lett.*, vol. 9, no. 4, pp. 3926–3931, Apr. 2024.